ADVANCED OPTICAL MATERIALS
www.advopticalmat.de

Pixel Geometry Effect on PbS Quantum Dot/Graphene Nanohybrid Broadband Photodetectors

Andrew Shultz, Bo Liu, Maogang Gong, Francisco C. Robles Hernandez, and Judy Wu**

Photodetectors based on colloidal quantum dots (QD)/graphene nanohybrids are quantum sensors due to strong quantum confinement in both QD and graphene. The optoelectronic properties of QD/graphene nanohybrids are affected by the quantum physics that predicts a high photoconductive gain and hence photoresponsivity (R^*) depending on the pixel length (L) as $R^* \propto L^{-2}$. Experimental confirmation of the effect of the pixel geometric parameters on the optoelectronic properties of the QD/graphene photodetector is therefore important to elucidate the underlying quantum physics. Motivated by this, an array of PbS QDs/graphene nanohybrid photodetectors are designed with variable QD/graphene pixel length L and width (W) in the range of 10–150 µm for a study of R^*, noise, and specific detectivity (D^*) in a broad spectrum of 400–1500 nm. Intriguingly, R^* exhibits a monotonic decreasing trend of $1/L^2$ while being independent of W, confirming experimentally the theoretical prediction. Interestingly, this geometric effect on the photoresponsivity seems to be partially compensated by that in noise, leading to D^* independent of L and W at wavelengths in the ultraviolet-visible-near infrared range. This result sheds light on the quantum physics underlying the optoelectronic process in QD/graphene nanohybrids, which is important to the design of high-quality QD/graphene photodetectors and imaging systems.

1. Introduction

Recent progress in optoelectronic devices utilizing the quantum dots (QD)/graphene nanohybrid heterostructure have been able to achieve high-efficiency solar cells[1] as well as high-performance broadband photodetectors,[2] both have shown promising performance due to the recent progress made in fabrication, characterization and applications of nanohybrids.[3–12] The QD/graphene nanohybrids can be readily incorporated into flexible media such as polyethylene terephthalate[13] and even cotton.[14] Interest in these nanohybrids has been growing for a decade since the first report on this architecture, using PbS QDs, achieved a D^* of 7×1013 Jones for illumination by a 600 nm laser with a gate voltage of −20 V.[15] Recent work by Grotevent et al found that D^* can be improved by an order of magnitude by cooling a PbS QD/graphene device to > 1010 Jones at 1280 nm wavelength from room temperature to 80 K.[16] Advancements in PbS QD synthesis techniques have achieved QDs as large as 15.3 nm with an absorption peak at 2460 nm and by use of a vertical diode structure reached a D^* of 1010 and 1011 Jones for 1500 and 2100 nm illumination, respectively.[17] This architecture remains very promising for next-generation optoelectronics.

The QD/graphene nanohybrid is a quantum device due to the strong quantum confinement in both QDs and graphene. The spectral tunability by QD size is a result of the quantum confinement in the QDs that also leads to suppressed phonon scattering and enhanced light-matter interactions.[18–21] For example, the absorption cutoff or bandgap of PbS QDs can be tuned by the QD size ranging from near-infrared to shortwave infrared, which can be tuned by varying the size of the QDs. The exciton (electron-hole pair) is generated when the incident light is absorbed by QDs in which a higher binding energy of up to a few hundreds of milli-eVs is expected from the strong quantum confinement, approximately an order of magnitude higher than in the conventional semiconductor bulks and films. This results in a larger exciton lifetime (τ_c) or reduced charge recombination.[22] Graphene, a 2D single atomic sheet of carbons atoms arranged in a hexagonal lattice, also exhibits quantum confinement at the 2D limit resulting in so-called Dirac fermions with Fermi velocity of 1/300 of light speed and hence high carrier mobility (μ) for massless fermions (both electrons and holes).[7,23–26] Stacking

A. Shultz, B. Liu, M. Gong, J. Wu
Department of Physics and Astronomy
The University of Kansas
Lawrence, KS 66045, USA
E-mail: andjshultz@ku.edu; jwu@ku.edu

M. Gong, J. Wu
ZenoLeap LLC
Innovation Park
Lawrence, KS 66045, USA

F. C. R. Hernandez
Department of Mechanical Engineering Technology
Advanced Manufacturing Institute
University of Houston
Houston, TX 77204, USA

F. C. R. Hernandez
Department Department of Materials Science and NanoEngineering
Rice University
Houston, TX 77005, USA

The ORCID identification number(s) for the author(s) of this article can be found under https://doi.org/10.1002/adom.202302675

DOI: 10.1002/adom.202302675

QDs on graphene creates a van der Waals interface with a built-in electric field due to the band edge alignment that promotes the separation of excitons to free charges in the photosensitive QD layer, followed by the transfer of one kind of charge from QD to graphene.[27–29] The photoresponse is the change in resistance of the graphene channel arising from the photogating by the other kind of the charge trapped in the QD. The high photoresponse of these QD/graphene devices is attributed to a large photoconductive gain (G) emerging from the long exciton lifetime τ_c (due to quantum confinement in the QDs) and a short charge transit time (τ_t) between the source and drain electrodes (due to the high carrier mobility of graphene). During τ_c before charge recombination occurs, the transferred charge could make multiple trips between the source and drain electrodes during τ_t defined as $\tau_t = \frac{L^2}{V_{sd}\,\mu}$, where L is the QD/graphene pixel channel length, μ is the carrier mobility, and V_{sd} is the applied bias voltage between source and drain. Therefore, the QD/graphene nanohybrids are expected to have a large G that is proportional to τ_c/τ_t due to the high τ_c in QDs and low τ_t in graphene (high μ).

Quantitatively, G is directly affected by the pixel geometric parameters of the QD/graphene photodetectors. For example, a $1/L^2$ dependence can be directly derived from the definition of the gain, which means the photoresponsivity (R^*) that is linearly proportional to G would increase with decreasing L through a relationship of $R^* \propto 1/L^2$. Experimental confirmation of this geometric effect is important but has not been done to our knowledge. In addition, the figure of merit-specific detectivity (D^*) is defined as $D^* = \frac{R^*\sqrt{LW\Delta f}}{I_N}$, which raises a question on how the pixel geometric parameters, specifically L and the channel width (W), would affect the noise current density (S_N), from which the noise current (I_N) is found, and ultimately the D^*. Answering this question is important not only to understanding the quantum physics underlying the QD/graphene optoelectronic process but also to the design of QD/graphene nanohybrids photodetectors and imaging arrays for practical applications. Motivated by this, a PbS QDs/graphene nanohybrid photodetector array was designed with a variable pixel dimension of L and W in the range of 10–150 µm. Evaluation of R^*, noise, and D* was carried out in a broadband spectrum of ultraviolet-visible-near and shortwave infrared (UV–vis–NIR–SWIR). It has been found that R^* indeed follows a $1/L^2$ trend as expected theoretically while being independent of W. Furthermore, the noise in QD/graphene nanohybrids is dominated by the 1/f noise from the graphene channel and exhibits a geometric effect. Interestingly, the D^* seems to be independent of L and W at variable wavelengths in the UV–vis–NIR–SWIR spectrum at room temperature.

2. Results and Discussion

In order to determine the quality and size of the synthesized PbS QDs high-resolution TEM (HETEM) was employed as seen in **Figure 1a**. A simulated Fast Fourier Transform (FFT) is presented in Figure 1b along with the projection of the crystal structure based on the Crystallographic Information File (CIF) for PbS, which demonstrates a good match between the experimental results and the theoretical simulated projections. The statistical analysis of the PbS QD diameter using various magnifications on the TEM images shows that the average diameter of the PbS QDs is ≈ 8.4 nm (Figure 1c). However, it is important to note that the QD size has a broad distribution in the range of 2–20 nm with ≈60% of the PbS QDs having sizes between 2 and 6 nm. This indicates a broad bandgap as it is affected directly by the QD size. In addition, the small QD size range of 2–20 nm is also important for the suspension of PbS QDs as well as for uniformity of the PbS QD/graphene device performance.[15,30] Figure 1d shows the simulated PbS lattice based on the CIF file confirming that QDs have a halite crystal structure as anticipated for PbS.

Figure 2a presents the optical absorption spectrum of the synthesized PbS QDs, with a resonance peak at 1430 nm. Despite a minor cutoff shoulder at the wavelength of ≈1780 nm, a broadband absorption of the PbS QDs is exhibited for detecting incident light from UV to SWIR wavelengths. Figure 2b exhibits the Raman spectra taken on a representative graphene sample employed for the PbS QD/graphene nanohybrid with the two characteristic graphene bands, the G band at 1610 cm^{-1} and 2D band at 2740 cm^{-1} as indicated. The G band arises from the in-plane vibrational mode and the 2D band is the second order of the D band (at 1356 cm^{-1}) that corresponds to the A1g breathing mode of the hexagonal rings. The ratio of the 2D and G band intensities (measured from the background to the top of the peak) is an indication of the layer count of the graphene.[31–33] Generally, a 2D/G band intensity ratio below 1 is considered few-layer graphene, between 1 and 1.4 is bilayer graphene, and higher for monolayer graphene. Figure 2c,d display a Raman map and the corresponding histogram of the 2D/G ratio, respectively, as well as an inset of the D/G ratio. From the 2D/G and D/G band intensity ratio distributions, we obtained the means and standard deviations of 1.47 ± 0.4 and 0.32 ± 0.13, respectively. It can be concluded the graphene is mostly monolayer with minor amounts of bilayer or few-layer, likely at the interconnects between graphene grains or folding of graphene from the transfer process. The concentration of defects in the crystal lattice is low as indicated by the low D/G band intensity ratio.[34] Thus the graphene is of suitable quality and uniformity for an array of devices to study the geometric effect on PbS QD/graphene optoelectronic properties.

Figure 3a illustrates schematically the PbS QD/graphene nanohybrid and the built-in electric field (E) associated to the band-edge alignment at the QD/graphene interface (Figure 3b). It should be noted that the as-grown CVD graphene is typically p-doped due to the presence of growth defects and the adsorption of polar molecules from the ambient air and processing chemicals as reported previously.[35] This explains the down-shift of the fermi level in graphene below the Dirac point, which makes hole transfer from PbS QD to graphene more favorable as shown in Figure 3b. Under incident light, the PbS QDs are expected to absorb the photons of energy exceeding the optical cutoff of the QDs. The excitons could dissociate into free electrons and holes with the assistance of the QD/graphene interface built-in electric field which can in turn drive the hole transfer from PbS QD to graphene as shown in Figure 3c. Within τ_c before charge recombination occurs, the electrons will be trapped inside the PbS QD while the transferred holes are making multiple trips between source and drain electrodes under the applied V_{sd} as illustrated in Figure 3d. The τ_t during each trip is defined as:

$$\tau_t = \frac{L^2}{\mu V_{sd}} \quad (1)$$

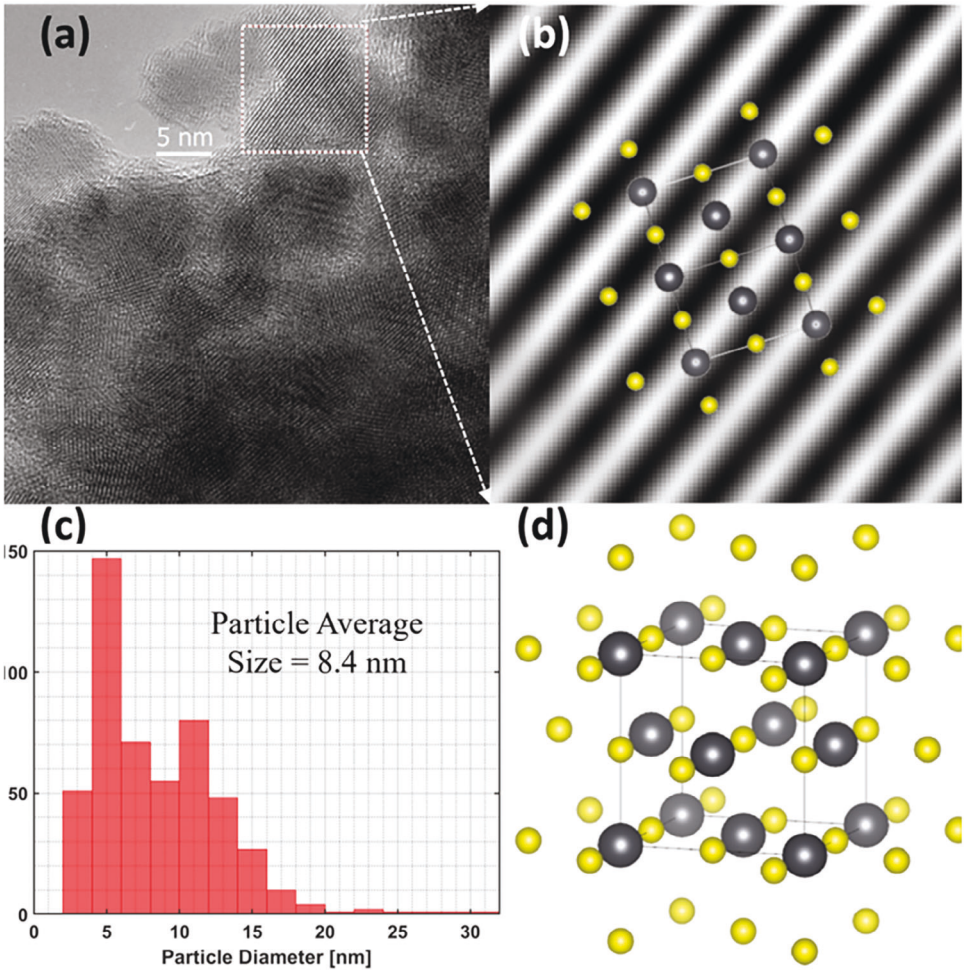

Figure 1. a) HETEM image of the PbS QDs. b) The corresponding FFT images of PbS QDs. c) The statistics of diameters of the PbS QDs. d) simulated PbS lattice based on the CIF file for PbS nanocrystals.

Dependence of τ_t on L arises from the drift velocity, $v = \frac{\mu V_{sd}}{L}$, in conjunction with the distance-velocity relationship in regard to time, $\tau_t = \frac{L}{v}$. It should be noted that V_{sd} needs to be consistent for all devices to observe the expected L dependence. The photoconductive gain of the QD/graphene nanohybrids is defined as the ratio of exciton lifetime to the carrier transit time:

$$G = \frac{\tau_c}{\tau_t} \tag{2}$$

Therefore, a large Gain exceeding 1010 could be obtained due to a large τ_c and a small τ_t enabled by the quantum confinement in the QDs and graphene, respectively. Furthermore, since charge transfer is a critical step in the optoelectronic process in the QD/graphene nanohybrids, the charge transfer blocking layer, such as the long-chain, insulating OLA ligands attached to the PbS QDs from the synthesis solution (Figure 3e) must be replaced with conductive MPA ligands (Figure 3f).

To investigate the pixel geometric effect, a 5×5 array of overall dimensions of 11×11 mm^2 (**Figure** 4a) was designed with variable pixel dimensions. Specifically, five L values of 10, 30, 50, 70, and 90 μm and five W values of 20, 40, 70, 100, and 150 μm were selected as shown in Figure 4b. It should be noted that the pixel dimension range was selected primarily considering it is commonly used for practical applications, making it important to probe the effect of pixel dimension on the device performance. A zoom-in view of the pixel of LxW = 90×150 μm is shown in Figure 4c. The overall length of the graphene strips is 220 μm, the contact area between graphene and the metal electrodes is 19500 μm2 for the case shown in Figure 4c. Figure 4d,e displays images of the 25 graphene channels (still covered with photoresist) and the fabricated 5×5 arrays of PbS QD/graphene nanohybrids. The substrate is electrically isolated (floating, no gate) and the doping on each graphene channel is primarily from polar air molecules adsorbed on the surface of graphene.[36,37] These polar molecules could be reduced/removed using a light-assisted vacuum annealing technique for an extended period, as shown in Figure S5 (Supporting Information), resulting in a shift of the Dirac point toward Vg = 0 as the p-doping by the polar air molecules is reduced. It should be noted that the 25 graphene channels investigated in this work are within a small area of 1×1 mm^2 at the center of the sample. This means the difference in p-doping by the polar air molecules is unlikely to differ largely from device to device. In addition, the moderate variance

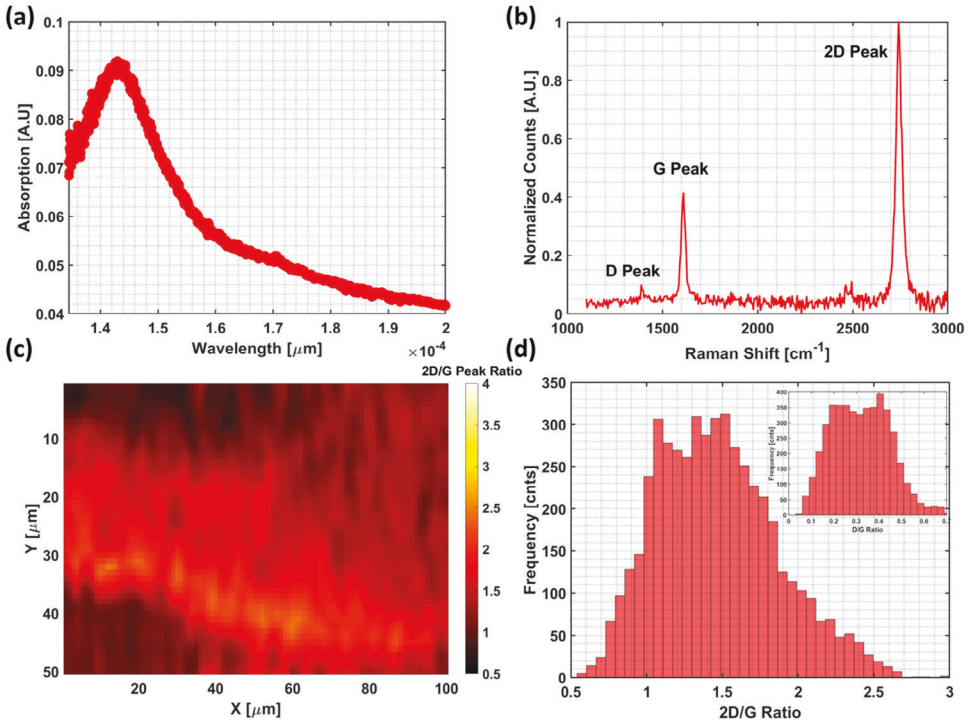

Figure 2. a) Optical absorption spectrum of the PbS QDs used in this study, with an absorption peak at 1.43 μm and cutoff wavelength at ≈1.78 μm. b) Representative Raman spectrum was taken on the graphene used for device fabrication. c,d) Map and histogram, respectively, of the Raman 2D/G peak ratio showing the graphene to be mostly monolayer with patches of bilayer (likely interconnects between monolayer grains). The inset displays the Raman D/G peak ratio histogram.

in conductance of the graphene channel from device to device is expected to have minor deviation if highly uniform graphene is used and great care is taken during the transfer process to minimize damage to the graphene. The range of L and W is suitable for discerning the trend of the figures of merit as a function of channel geometry given small variations in the graphene quality and conductance.

R^* is defined as the ratio of photocurrent (current with illumination, I_L, minus the current in the dark, I_D) to the power of the light incident (P_0) on the device (with η being the quantum efficiency, e the electron charge, and G the photoconductive gain):[38]

$$R^* = \frac{I_L - I_D}{P_0} = \frac{e\eta G}{P_0} \tag{3}$$

Thus R^* is expected to vary with channel length as L^2, from G, while remaining independent of the channel width based on Equations (1)–(3). The measured R^* (V_{sd} = 0.5 V) as a function of W and L for the 5×5 varied geometry array is shown under three different incident light wavelengths of 400 nm (**Figure** 5a,b), 1000 nm (Figure 5c,d) and 1500 nm (Figure 5e,f), respectively. At all three wavelengths selected from the UV-vis-NIR-SWIR spectra, the R^* exhibits negligible trends of W dependence as shown in Figure 5a,c,e. In contrast, a monotonic decreasing trend with increasing L is clearly visible, which can be fitted with $1/L^2$ (dotted lines in Figure 5b,d,f). This verifies the theoretically predicted channel length dependence of G and hence R^* in the QD/graphene nanohybrids. Note the three wavelengths selected to cover a broadband from visible (400 nm), to near-infrared (1000 nm), and to SWIR (1500 nm). This result hence illustrates the same quantum physics applies to the broadband spectra and R^* can be maximized by simply decreasing the channel length as much as possible.

In conventional semiconductor photodetectors, D^* is the figure of merit for photodetectors due to the accounting for geometric factors and noise to produce a quantity that can be used to directly compare photodetectors comprised of different materials as well as detector geometric parameters.[39,40] D^* is defined as,

$$D^* = \frac{\sqrt{A\Delta f}}{NEP} = \frac{R^*\sqrt{LW\Delta f}}{I_N} \tag{4}$$

where $NEP = I_N/R^*$ is the noise equivalent power, A is the channel area, Δf is the bandwidth (1 Hz), and I_N is the noise current in A. In the above equation, we can see that the L^2 factor from R^* is not canceled out by the $\sqrt{L}$. The $\sqrt{LW}$ dependence is used to cancel out the geometric dependence of shot noise. If D^* is to be independent of pixel geometric parameters in the QD/graphene nanohybrids, we expect that S_N should be proportional to L and W as,

$$I_N \propto S_N \propto \frac{W^{\frac{1}{2}}}{L^{\frac{3}{2}}} \tag{5}$$

The experimentally measured S_N of a PbS QD/graphene nanohybrid device before (red) and after (orange) the PbS QD deposition, and after the MPA ligand exchange (blue) are compared in **Figure** 6a for a device channel geometry LxW = 0.2×4 mm

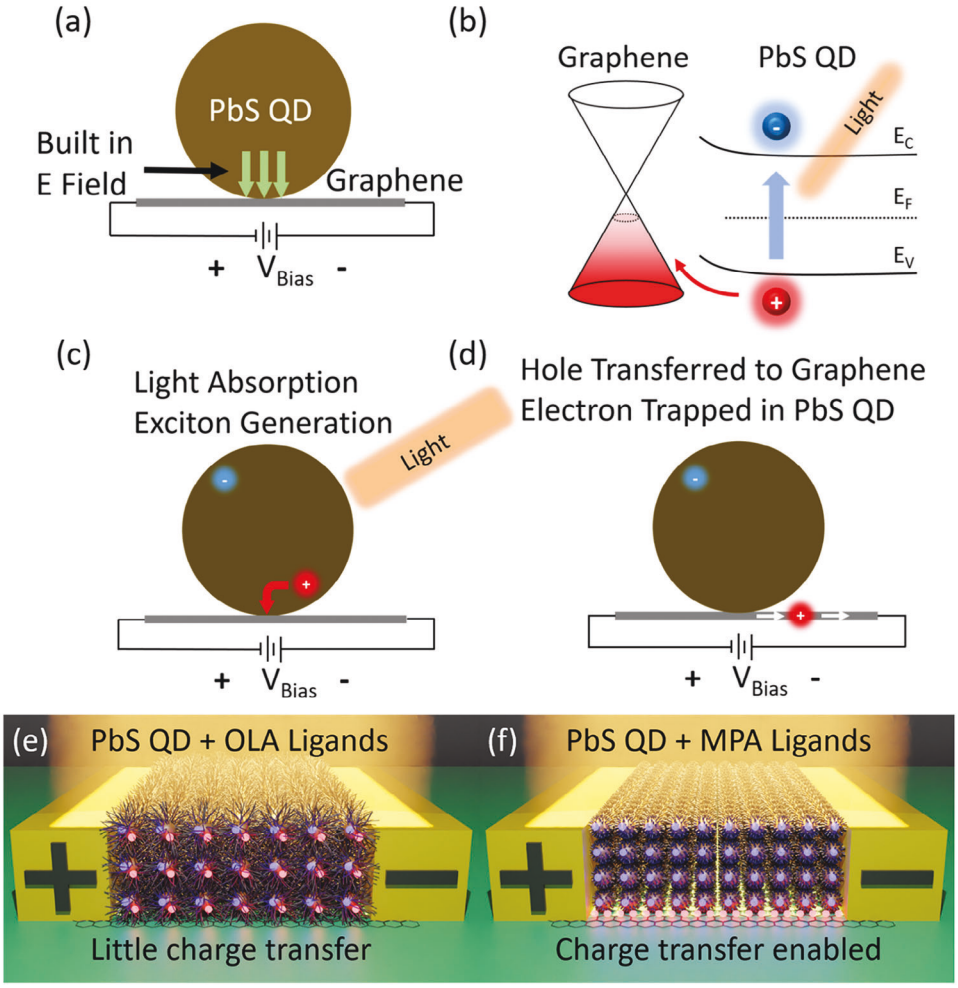

Figure 3. a) Charge transfer schematic at the QD/graphene interface associated with (b) the built-in electric field (E) due to the band-edge alignment at the interface. c) Exciton generation upon light absorption and dissociation assisted by the built-in electric field followed by (d) charge transfer to graphene for circulation before recombination. Artistic visualization of the device operation with (e) insulating OLA ligands and (f) conducting MPA ligands.

using a bias voltage of 0.5 V. At low frequencies (< ≈100 kHz) noise in graphene is dominated by flicker noise (1/f) which is thought to be the result of charge mobility fluctuations.[41,42] The change of the S_N before and after the PbS QD deposition is negligible, suggesting the noise in the QD/graphene nanohybrids is dominated by the noise in graphene. Interestingly, a considerable reduction of the S_N at low frequencies up to ≈ 400 Hz has been observed after MPA ligand exchange, which may be attributed to the modification of the PbS QD/graphene interface and the possible de-doping of graphene by partially removing the adsorbed polar molecules. This argument is consistent with the slight increase in graphene channel resistance by a factor of ≈ 1.2 after the MPA ligand exchange. Figure 6b compares the noise spectra of the PbS QD/graphene nanohybrids measured in dark (red) and exposed to broadband illumination (blue). Interestingly, comparable and slightly lower noise is shown under light, which indicates the noise in the graphene channel is only moderately affected by the photo-generated carriers. Figures 6c,d exhibit the S_N measured from all 25 channels of the 5×5 array as a function of L and W, respectively (Figure S4 (Supporting Information) has the same data plotted versus $W^{1/2}L^{-3/2}$ to show the linear trend). The fit lines conform quite well to the anticipated $W^{1/2}$ and $L^{-3/2}$ trends for the noise current, which indicates the independence of D^* from pixel geometric parameters in the PbS QD/graphene nanohybrids photodetectors similar to the case of conventional photodetectors.[43,44]

This projection is confirmed in the D^* versus pixel width and length plots shown in **Figure** 7a at 400 nm wavelength, Figure 7b at 1000 nm wavelength, Figure 7c at 1500 nm wavelength, respectively. The error bars in Figure 7 are found from the average and standard deviation of D^* of all devices with the same length or width. Figure 7d contains the light intensity dependence of D^* at different wavelengths in the range of 400–1500 nm. A monotonic decreasing trend of D^* with light intensity can be seen at all wavelengths as reported for nanohybrids.[13,15,45] The highest D^* obtained is on the order of 1010 (1500 nm) −1012 (400 nm) Jones at room temperature, which is of the same order of magnitude as our previously published work on QD/graphene nanohybrid

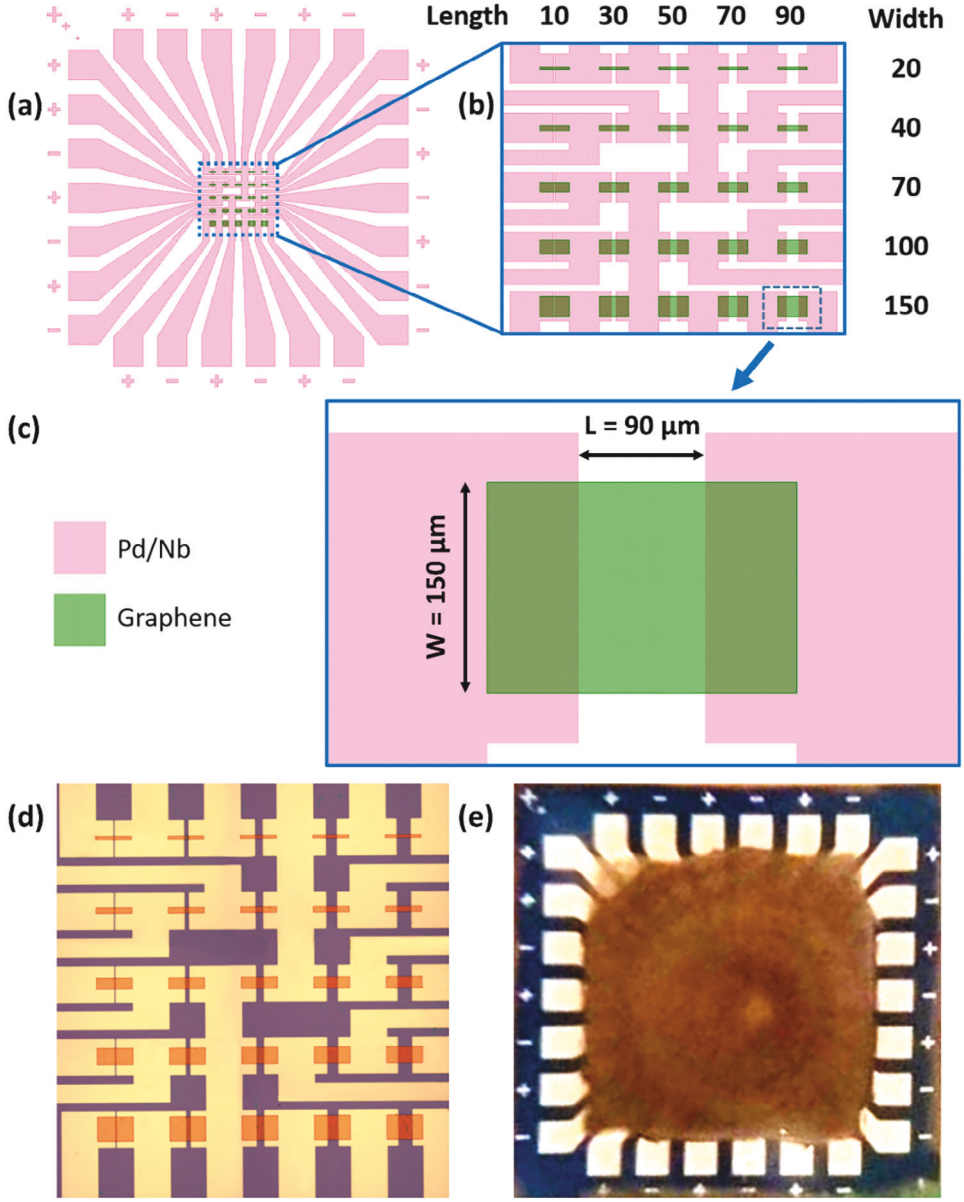

Figure 4. a) A 5×5 QD/graphene device array (overall dimension: 11×11 mm^2) with variable pixel geometry of channel width and length. b) Zoom-in view of the 25 devices with varied L values of 10, 30, 50, 70, and 90 µm and W values of 20, 40, 70, 100, and 150 µm, respectively. c) Schematic of a single device showing the definitions of L and W. d) The fabricated 5×5 arrays prior to liftoff of the photoresist used to define the graphene channels and QD deposition. e) Fully fabricated 5×5 array before wiring to a chip carrier.

using PbS.[13] By comparison, the R^* for 100 µm channel lengths under 1000 nm irradiation is on the order of 102 A W^{-1}, close to the reported value by Sun et al for 0 V gate voltage under 895 nm with similar intensity.[45] The first report on the QD/graphene architecture (utilizing PbS QDs) by Konstantatos et al obtained an R^* of ≈107 A W^{-1} with a 10 µm channel length for 600 nm photons, 4 µW cm^{-2} intensity, and a gate of −20 V.[15] Comparing our R^* of ≈105 A W^{-1} for 550 nm, 18 µW cm^{-2} intensity, and no applied gate, to the work of Konstantatos et al we find 2 orders of magnitude difference that can be explained by: (1) the use of a gate to optimize the charge transfer from QD to graphene (2) lower light intensity and (3) smaller QDs, which are better at trapping charges and thus achieve a higher photoconductive gain. We estimate that (1) through (3) would account for two orders of magnitude and would put our results on par with that of Konstantatos et al.

3. Conclusion

In summary, a 5×5 array of PbS QD/graphene nanohybrids photodetectors was fabricated and characterized to elucidate the effect of variable pixel length L and width W on the optoelectronic

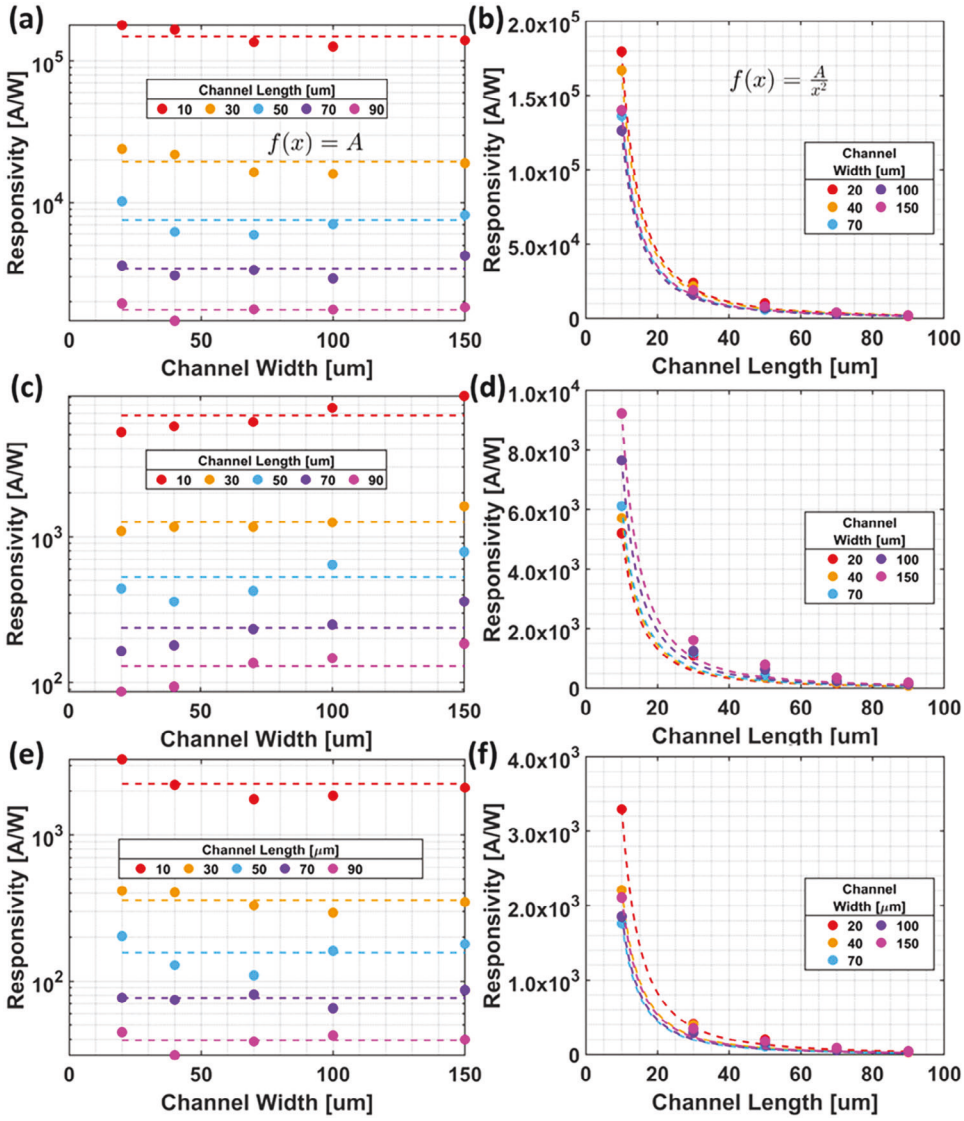

Figure 5. Responsivity (V_{sd} = 0.5 V) as a function of channel width and length, respectively, for incident light of wavelengths of a,b) 400 nm with an intensity of 13 μW cm^{-2}, c,d) 1000 nm with an intensity of 150 μW cm^{-2}, and e,f) 1500 nm with an intensity of 280 μW cm^{-2}.

properties (R^*, S_N, and D^*) of the device. Specifically, L values of 10, 30, 50, 70, and 90 μm and W values of 20, 40, 70, 100, and 150 μm were designed into an array to examine the theoretically predicted pixel geometric dimension dependence of photoconductive gain and hence R^* on QDs/graphene nanohybrids based on the physics in this quantum sensor. The R^*, S_N, and D^* were evaluated on the 25 channels of PbS QD/graphene nanohybrids of different geometric dimensions in a broadband incident light of 400–1500 nm. Several critical insights have been obtained. First, the R^* has been confirmed to depend on $1/L^2$, which means the strong quantum confinement in QD and graphene indeed governs the gain and hence R^* as expected from theory. On the other hand, no W dependence was observed on R^*, which is not surprising since no W dependence is predicted by theory. Furthermore, the S_N in the QD/graphene nanohybrids has been found to be dominated by the noise from graphene, which is 1/f noise at low frequencies of 1–1000 Hz. Negligible effects from the deposited PbS QDs either in dark or in light on the noise of the QD/graphene nanohybrids were observed. Furthermore, a moderate reduction of the S_N has been observed via MPA ligand exchange, suggesting that de-doping of graphene may lead to further reduced noise toward its intrinsic limit. Interestingly, the S_N exhibits a pixel dimension dependence of $L^{-3/2}$ and $W^{1/2}$, resulting in the geometric dimension independent D^* values. A remarkably high D^* of 1010 –1012 Jones has been obtained in the broadband spectrum of 400–1500 nm at room temperature, making QD/graphene nanohybrids promising candidates for high-sensitivity and low-cost photodetectors and imaging systems.

4. Experimental Section

Fabrication of QD/Graphene Nanohybrid Devices: Fabrication of the QD/graphene nanohybrid devices began with cleaning the SiO_2 (500 nm)/Si substrates using 3 rinsing cycles of acetone, isopropanol,

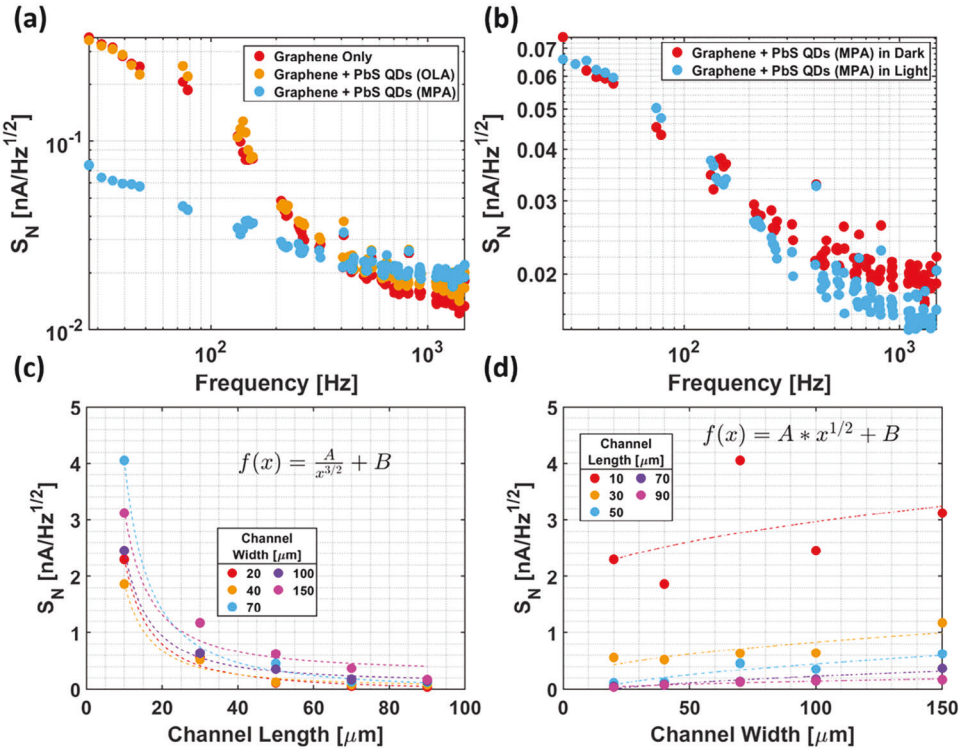

Figure 6. a) Noise spectra for a PbS QD/graphene device at different stages in the device fabrication process including before (red) and after (orange) PbS QD deposition, followed by MPA ligand exchange (blue). b) Noise spectra for a PbS QD/graphene device in the dark (red) and under the illumination of a high-intensity broadband light source (blue). The device geometry for (a) and (b) is 0.2 mm (L) x 4 mm (W) with a bias voltage of 0.5 V. c,d) Noise current density dependence on channel length and width, respectively, at 100 Hz.

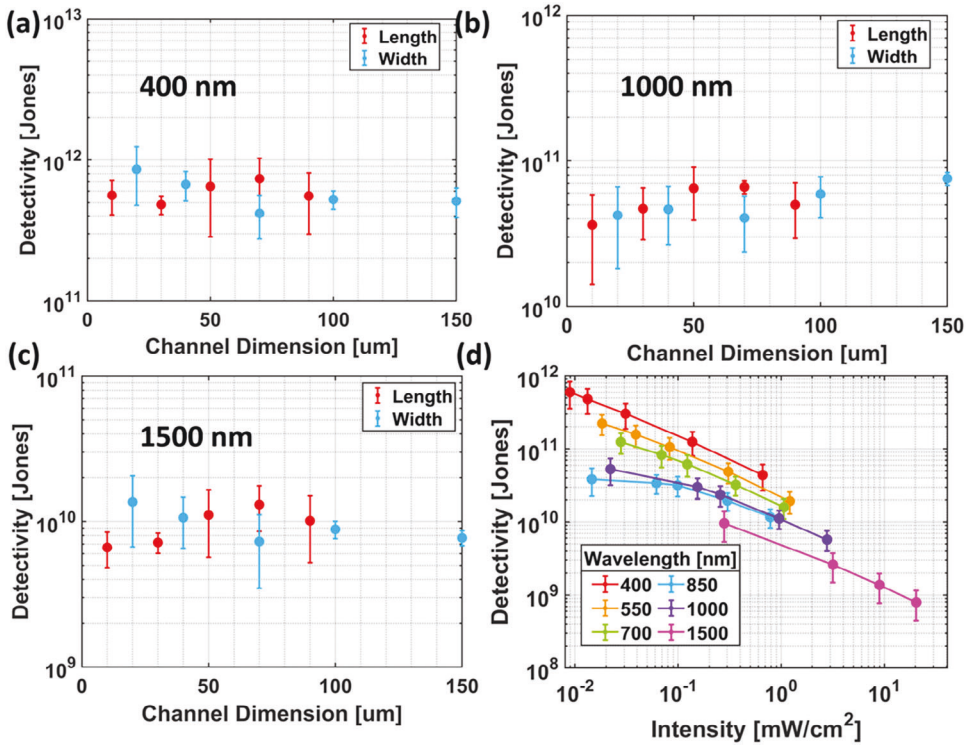

Figure 7. a–c) Detectivity as a function of channel width and length for illumination by 400 nm with an intensity of 13 μW cm^{-2}, 1000 nm with an intensity of 150 μW cm^{-2}, and 1500 nm with an intensity of 280 μW cm^{-2}. d) Detectivity as a function of intensity for a few different wavelengths.

and reverse osmosis water. Two standard photolithography steps were applied to define the metal electrodes and graphene channels respectively. The first photolithography was performed on the bare SiO_2 (500 nm)/Si substrates. Deposition of the electrodes for the 5×5 arrays was carried out using a photomask-generated pattern followed by DC sputtering in a high vacuum chamber (base pressure of 2.5×10^{-7} Torr). The deposited electrodes are 40 nm Nb followed by 10 nm of Pd from the Nb and Pd targets (ACI Alloys). The working gas was Ar (99.999%) at a pressure of 14 mTorr/30 mTorr with a sputtering power of 75 W/87 W for Nb/Pd, respectively. Single-layer graphene was grown on polycrystalline copper foil with a thickness of 50 µm (Sigma–Aldrich) using low-pressure chemical vapor deposition (CVD) at 1050 °C with H_2/CH_4 gases following the previously reported method.[31] The graphene was wet transferred onto the prefabricated Nb/Pd electrodes (after the liftoff) using a wet transfer method reported previously.[35,46] The second photolithography was carried out to define the graphene channels, followed with reactive ion etching (RIE) of unwanted graphene in oxygen plasma in an RF RIE system (Torr International) at a pressure of 8 mTorr and 20 W RF power for 2 min.

PbS QDs were synthesized in an Ar environment in a Schlenk line system and the details were reported previously.[47] The PbS QDs were suspended in hexane with a mixture of 1:1. A Bioforce Nanosciences UV/Ozone ProCleaner was used prior to QD deposition for specified samples. Deposition of the QDs was carried out by a micropipette to transfer 10 µL of suspended PbS QDs onto the substrate. A spin coater, operated at 3000 RPM for 1 min, was employed to obtain a thin uniform film of PbS QDs over the center area of the 5×5 arrays. Efficient charge transfer from the QDs to the graphene, as well as from QD to QD, is integral for superior device performance.[22,48] In order to facilitate charge transfer, the insulating long-chain ligands of Oleylamine (OLA) and Oleic Acid (OA) that encapsulate the QDs from the synthesis procedure (which also serve to prevent QD degradation during storage) must be exchanged with more conductive ones. Ligand exchange is carried out by exposing the QDs to 3-mercaptopropionic acid (MPA) to replace the OLA and OA ligands.[49] After coating PbS QDs on the substrate, 20 µL of MPA and methanol (1:1 mixture) was dropped on the substrate followed by a 1 min wait period with subsequent removal of the MPA/methanol mixture by spin coating at 3000 RPM for 1 min. Lastly, residual MPA was rinsed off using 20 µL of methanol followed by spin coating with the same parameters again. Rinsing with methanol was carried out twice. Finally, the platinum wires (50 µm in diameter) were soldered to the electrodes on the substrate and the pins of the chip carrier that can then be plugged into the readout electronics.

Sample Characterization: The optical absorption spectrum of PbS QDs was collected using a UV-3600 Shimadzu spectrometer. The crystal structure and morphology of the PbS QDs were characterized using a field-emission transmission electron microscope (FETEM) on a JEOL 2100 system with an accelerating voltage of 200 kV. Raman spectra were taken on graphene with a WiTec Alpha300 confocal micro-Raman system using a 488 nm excitation laser. PbS QD film thickness was measured with a KLA Tencor P-16 profiler. Noise spectra were taken using a Stanford Research Systems SR760 FFT Spectrum Analyzer and a home-built battery-operated DC power supply with a bias voltage in the range of 0 to 0.5 V.

Optoelectronic Characterization of PbS QD/Graphene 5×5 Array: A Newport Oriel Apex Monochromator Illuminator white light source and a Newport Oriel Cornerstone 130 1/8m Monochromator were used to measure the spectral responsivity from 400 to 1000 nm. A SEI SLA5653 diode laser was used as the light source for 1.5 µm wavelength in the SWIR. The diode lasers were powered by an Arroyo Instruments 6310 power supply. The light sources were modulated using a Thorlabs MC1000 optical chopper and the resulting device photocurrent was measured by a CH Instruments 660D electrochemical workstation with an applied V_{sd} = 0.5 V. The devices were tested with the substrate electrically isolated (floating, no gate).

Supporting Information

Supporting Information is available from the Wiley Online Library or from the author.

Acknowledgements

This research was supported by the US Army Grant (W909MY-21-C-0033).

Conflict of Interest

The authors declare no conflict of interest.

Data Availability Statement

The data that support the findings of this study are available from the corresponding author upon reasonable request.

Keywords

detectivity, geometry, graphene, nanohybrid photodetector, noise, quantum dots, responsivity

Received: October 20, 2023
Revised: February 21, 2024
Published online: March 14, 2024

[1] L. Najafi, B. Taheri, B. Martin-Garcia, S. Bellani, D. Di Girolamo, A. Agresti, R. Oropesa-Nunez, S. Pescetelli, L. Vesce, E. Calabro, *ACS Nano* **2018**, *12*, 10736.
[2] V. K. Singh, S. M. Yadav, H. Mishra, R. Kumar, R. Tiwari, A. Pandey, A. Srivastava, *ACS Appl. Nano Mater.* **2019**, *2*, 3934.
[3] F. H. Koppens, T. Mueller, P. Avouris, A. C. Ferrari, M. S. Vitiello, M. Polini, *Nat. Nanotechnol.* **2014**, *9*, 780.
[4] Z.-Y. Peng, J.-L. Xu, J.-Y. Zhang, X. Gao, S.-D. Wang, *Adv. Mater. Interfaces* **2018**, *5*, 1800505.
[5] C. Xie, F. Yan, *Small* **2017**, *13*, 1701822.
[6] J. Wu, Y. Lu, S. Feng, Z. Wu, S. Lin, Z. Hao, T. Yao, X. Li, H. Zhu, S. Lin, *Adv. Funct. Mater.* **2018**, *28*, 1804712.
[7] A. K. Geim, *Science* **2009**, *324*, 1530.
[8] A. K. Geim, I. V. Grigorieva, *Nature* **2013**, *499*, 419.
[9] F. N. Xia, H. Wang, D. Xiao, M. Dubey, A. Ramasubramaniam, *Nat. Photonics* **2014**, *8*, 899.
[10] F. H. L. Koppens, T. Mueller, P. Avouris, A. C. Ferrari, M. S. Vitiello, M. Polini, *Nat. Nanotechnol.* **2014**, *9*, 780.
[11] F. Bonaccorso, Z. Sun, T. Hasan, A. C. Ferrari, *Nat. Photonics* **2010**, *4*, 611.
[12] F. Xia, H. Wang, D. Xiao, M. Dubey, A. Ramasubramaniam, *Nat. Photonics* **2014**, *8*, 899.
[13] A. Shultz, B. Liu, M. Gong, M. Alamri, M. Walsh, R. C. Schmitz, J. Z. Wu, *ACS Appl. Nano Mater.* **2022**, *5*, 16896.
[14] Abid, P. Sehrawat, C. Julien, S. Islam, *ACS Appl. Mater. Interfaces* **2020**, *12*, 39730.
[15] G. Konstantatos, M. Badioli, L. Gaudreau, J. Osmond, M. Bernechea, F. P. G. de Arquer, F. Gatti, F. H. L. Koppens, *Nat. Nanotechnol.* **2012**, *7*, 363.
[16] M. J. Grotevent, C. U. Hail, S. Yakunin, D. Bachmann, G. k. Kara, D. N. Dirin, M. Calame, D. Poulikakos, M. V. Kovalenko, I. Shorubalko, *ACS Appl. Mater. Interfaces* **2020**, *13*, 848.
[17] C. Dong, S. Liu, N. Barange, J. Lee, T. Pardue, X. Yi, S. Yin, F. So, *ACS Appl. Mater. Interfaces* **2019**, *11*, 44451.
[18] D. Debellis, G. Gigli, S. Ten Brinck, I. Infante, C. Giansante, *Nano Lett.* **2017**, *17*, 1248.
[19] J. Tang, K. W. Kemp, S. Hoogland, K. S. Jeong, H. Liu, L. Levina, M. Furukawa, X. Wang, R. Debnath, D. Cha, K. W. Chou, A. Fischer, A. Amassian, J. B. Asbury, E. H. Sargent, *Nat. Mater.* **2011**, *10*, 765.

[20] A. H. Ip, S. M. Thon, S. Hoogland, O. Voznyy, D. Zhitomirsky, R. Debnath, L. Levina, L. R. Rollny, G. H. Carey, A. Fischer, K. W. Kemp, I. J. Kramer, Z. Ning, A. J. Labelle, K. W. Chou, A. Amassian, E. H. Sargent, *Nat. Nanotechnol.* **2012**, *7*, 577.
[21] H. Lu, G. M. Carroll, N. R. Neale, M. C. Beard, *ACS Nano* **2019**, *13*, 939.
[22] J. Wu, M. Gong, R. C. Schmitz, B. Liu, In *Quantum Dot Photodetectors*, Vol. *30*, Springer, Cham, **2021**, pp. 215–248.
[23] C. R. Dean, A. F. Young, I. Meric, C. Lee, L. Wang, S. Sorgenfrei, K. Watanabe, T. Taniguchi, P. Kim, K. L. Shepard, J. Hone, *Nat. Nanotechnol.* **2010**, *5*, 722.
[24] J. H. Chen, C. Jang, S. D. Xiao, M. Ishigami, M. S. Fuhrer, *Nat. Nanotechnol.* **2008**, *3*, 206.
[25] A. K. Geim, K. S. Novoselov, *Nat. Mater.* **2007**, *6*, 183.
[26] J. Wu, H. Ma, P. Yin, Y. Ge, Y. Zhang, L. Li, H. Zhang, H. Lin, *Small Sci.* **2021**, *1*, 2000053.
[27] H. Xu, J. Wu, Q. Feng, N. Mao, C. Wang, J. Zhang, *Small* **2014**, *10*, 2300.
[28] F. Koppens, T. Mueller, P. Avouris, A. Ferrari, M. Vitiello, M. Polini, *Nat. Nanotechnol.* **2014**, *9*, 780.
[29] H. Geng, D. Yuan, Z. Yang, Z. Tang, X. Zhang, K. Yang, Y. Su, *J. Mater. Chem. C* **2019**, *7*, 11056.
[30] I. Moreels, K. Lambert, D. Smeets, D. De Muynck, T. Nollet, J. C. Martins, F. Vanhaecke, A. Vantomme, C. Delerue, G. Allan, *ACS Nano* **2009**, *3*, 3023.
[31] Y. G. Qingfeng Liu, J. S. Wilt, R. Sakidja, J. Wu, *Carbon* **2015**, *93*, 199.
[32] L. Liu, H. Zhou, R. Cheng, W. J. Yu, Y. Liu, Y. Chen, J. Shaw, X. Zhong, Y. Huang, X. Duan, *ACS Nano* **2012**, *6*, 8241.
[33] K. Yan, H. Peng, Y. Zhou, H. Li, Z. Liu, *Nano Lett.* **2011**, *11*, 1111.
[34] C. Rochford, N. Kumar, J. Liu, H. Zhao, J. Wu, *ACS Appl. Mater. Interfaces* **2013**, *5*, 7176.
[35] G. Xu, R. Lu, J. Liu, H. Y. Chiu, R. Hui, J. Z. Wu, *Adv. Opt. Mater.* **2014**, *2*, 729.
[36] R. Lu, J. Liu, H. Luo, V. Chikan, J. Z. Wu, *Sci. Rep.* **2016**, *6*, 19161.
[37] Z. Yong, G. Hu, M. Gong, M. Alamri, C. Ma, M. Liu, J. Wu, *Adv. Mater. Interfaces* **2018**, *6*, 1801380.
[38] A. Rogalski, *ACS Photonics* **2023**, *10*, 647.
[39] X. Liu, Y. Lin, Y. Liao, J. Wu, Y. Zheng, *J. Mater. Chem. C* **2018**, *6*, 3634.
[40] G. Simone, M. J. Dyson, S. C. Meskers, R. A. Janssen, G. H. Gelinck, *Adv. Funct. Mater.* **2020**, *30*, 1904205.
[41] A. N. Pal, S. Ghatak, V. Kochat, E. Sneha, A. Sampathkumar, S. Raghavan, A. Ghosh, *ACS Nano* **2011**, *5*, 2075.
[42] A. A. Balandin, *Nat. Nanotechnol.* **2013**, *8*, 549.
[43] A. Rose, *Helvetica. Physica. Acta.* **1957**, *30*, 242.
[44] R. C. Jones, *JOSA* **1960**, *50*, 1058.
[45] Z. Sun, Z. Liu, J. Li, G. Tai, S. P. Lau, F. Yan, *Adv. Mater.* **2012**, *24*, 5878.
[46] M. Gong, M. Alamri, D. Ewing, S. M. Sadeghi, J. Z. Wu, *Adv. Mater.* **2020**, *32*, 2002163.
[47] M. G. Brent Cook, D. Ewing, M. Casper, A. Stramel, A. Elliot, J. Wu, *ACS Appl. Nano Mater.* **2019**, *2*, 3246.
[48] M. Gong, Q. Liu, B. Cook, B. Kattel, T. Wang, W. L. Chan, D. Ewing, M. Casper, A. Stramel, J. Z. Wu, *ACS Nano* **2017**, *11*, 4114.
[49] M. Gong, Q. Liu, R. Goul, D. Ewing, M. Casper, A. Stramel, A. Elliot, J. Z. Wu, *ACS Appl. Mater. Interfaces* **2017**, *9*, 27801.